Humidity Dependence of the Condensational Growth of Pinene Secondary Organic Aerosol Particles

Share Your Story

The Harvard community has made this article openly available.
Please share how this access benefits you. Submit a story .

Accessibility

Humidity Dependence of the Condensational Growth of α-Pinene Secondary Organic Aerosol Particles

Yiming Qin, Jianhuai Ye, Paul Ohno, Jinghao Zhai, Yuemei Han, Pengfei Liu, Junfeng Wang, Rahul A. Zaveri,* and Scot T. Martin*

ACCESS | Metrics & More | Article Recommendations | Supporting Information

ABSTRACT: The influence of relative humidity (RH) on the condensational growth of organic aerosol particles remains incompletely understood. Herein, the RH dependence was investigated via a series of experiments for α-pinene ozonolysis in a continuously mixed flow chamber in which recurring cycles of particle growth occurred every 7 to 8 h at a given RH. In 5 h, the mean increase in the particle mode diameter was 15 nm at 0% RH and 110 nm at 75% RH. The corresponding particle growth coefficients, representing a combination of the thermodynamic driving force and the kinetic resistance to mass transfer, increased from 0.35 to 2.3 $nm^2\ s^{-1}$. The chemical composition, characterized by O:C and H:C atomic ratios of 0.52 and 1.48, respectively, and determined by mass spectrometry, did not depend on RH. The *Model for Simulating Aerosol Interactions and Chemistry* (MOSAIC) was applied to reproduce the observed size- and RH-dependent particle growth by optimizing the diffusivities D_b within the particles of the condensing molecules. The D_b values increased from 5 $\alpha^{-1} \times 10^{-16}$ at 0% RH to 2 $\alpha^{-1} \times 10^{-12}\ cm^{-2}\ s^{-1}$ at 75% RH for mass accommodation coefficients α of 0.1 to 1.0, highlighting the importance of particle-phase properties in modeling the growth of atmospheric aerosol particles.

KEYWORDS: *atmospheric particles, aerosol particle growth dynamics, aerosol particle size distribution, mass accommodation coefficient, particle-phase diffusivity*
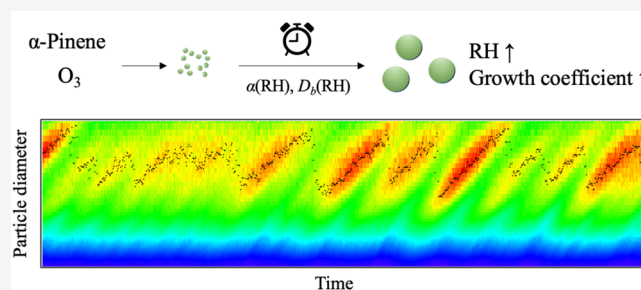
1. INTRODUCTION

The condensation of atmospheric semivolatile and low-volatility organic molecules from the gas phase onto particles plays an important role in the size evolution of the atmospheric particle population.[1,2] This continuous condensation of molecules makes particle size a moving target in atmospheric systems, and the impacts of aerosol particles on climate and human health depend strongly on particle diameter. Larger particles deposit in the upper portion of the human respiratory tract. Micron-sized particles penetrate deep into the lungs, leading to size-dependent respiratory effects.[3] The light scattering efficiency of submicron particles, resulting in a mechanism of direct radiative forcing in models of climate, is controlled principally by particle diameter.[4] The efficacy of particles to act as cloud condensation nuclei (CCN) and to affect cloud formation, serving as a mechanism of indirect radiative forcing, is driven by particle diameter.[5] The dominant mechanism of particle loss from the atmosphere and hence the number concentration of particles in the atmosphere depends on particle diameter.[6] An understanding of the factors that influence the condensational growth of particles is critical for estimating their environmental effects.

The condensable molecules are a downstream consequence of atmospheric oxidation of volatile organic compounds (VOCs) emitted from natural and human sources forming products of lower volatility.[7] The less-volatile compounds exit the gas phase by condensation onto particles, leading to the diameter growth of so-named secondary organic aerosol (SOA) particles. The less-volatile product compounds are classified by their saturation mass concentrations C^* over pure material.[8] Semivolatile and low-volatility organic compounds ($C^* \leq 10^{2.5}\ \mu g\ m^{-3}$) contribute strongly to the growth rate of submicron atmospheric organic particles (i.e., 100 to 1000 nm).[9]

The thermodynamic driving force for the condensation of semivolatile and low-volatility species from the gas phase onto organic particles is governed by the difference between the gas-phase concentration and the particle-phase saturation concentration of the condensable species.[2,10] Particle-phase reactions can further increase the net mass transfer of a condensing species.[11] For a given thermodynamic driving force, an upper limit of the condensation rate can be calculated.[6,12,13] The actual
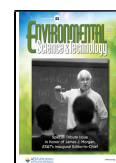
condensation rate can be less than the upper limit because of tempering by kinetic inhibition of mass transfer. Inhibition can occur both at the surface and within the particle, possibly including coupling to particle-phase reactions.[14−16] In some cases, kinetic inhibition can be so significant that the actual condensation rate and hence the growth rates are orders of magnitude less than the upper limit of the thermodynamic driving force. Many of the kinetic effects depend on relative humidity.[17,18] RH can influence gas-particle interactions because of RH-dependent diffusivity, especially in organic particles. Among other related studies, Gong et al.,[14] Han et al.,[10] Kuwata et al.,[19] Li et al.,[20] Perraud et al.,[21] and Zaveri et al.[17] observed that the uptake of gas-phase species onto particles is limited by low particle-phase diffusivity at sufficiently low RH. For low diffusivity, condensing species are not cleared fast enough from the surface region into the interior of the particles. Instead, they enrich the surface region and thus reduce the local driving force of further condensation, leading to slower particle growth. The tie-ins of atmospheric variability in RH to the process variability in the growth rate of atmospheric particles, including the mechanisms of that link through diffusivity, remain unclear and unquantified.

The present study investigates the RH dependence of the condensational growth rates of α-pinene-derived SOA particles. Repeated episodes of particle growth are observed in a continuously mixed flow reactor for stepwise changes in RH. The data sets are interpreted in the context of particle-phase diffusivity by the use of the *Model for Simulating Aerosol Interactions and Chemistry* (MOSAIC). The underlying mechanisms of the RH-dependent condensational growth are discussed.

2. EXPERIMENTAL SECTION

2.1. Chamber Experiments. Organic particles were produced from α-pinene ozonolysis in the Harvard Environmental Chamber (HEC).[22−24] The HEC consisted of a Teflon bag operated as a continuously mixed flow reactor (CMFR) housed within a temperature-controlled walk-in room. For the CMFR mode, air, water vapor, and ozone flows were mixed together upstream of the CMFR, and this mixed flow was continuously introduced into the center of the bag during the course of the experiments. Through a separate inlet, α-pinene (Sigma-Aldrich, ≥ 99%) was continuously injected perpendicular to and approximately 1 m away from the first inlet to promote mixing in the CMFR. Volumetric inflows and outflows of the bag were balanced by feedback control based on a constant but small overpressure on the chamber bag. Ozone and α-pinene reacted within the bag to produce a dynamic population of SOA particles. No particles were present in the inflow to the HEC, so all particles in the outflow arose from new particle production and subsequent condensational growth. The residence time distribution of individual particles inside the bag followed Poisson statistics. The volume of the Teflon bag was 4.7 m³, the flow rate was 18 L min⁻¹, and the Poisson mean residence time was 4.4 h.

Ozone was produced by exposing pure air to the ultraviolet emissions of a mercury lamp (185 nm). The ozone concentration was monitored by a photometric analyzer (model 400E, Teledyne). α-Pinene was produced from a syringe pump into a glass bulb, and it was carried by zero air into the HEC bag. In the absence of ozonolysis, the α-pinene concentration inside the bag was 22 ppbv. The concentrations were calculated based on the mass balance of the α-pinene and

the chamber flow. The real-time ozone concentration after reaction varied from 300 to 340 ppb during the course of different experiments, and the values for each experiment are plotted in Figure S1. The high ozone-to-α-pinene concentration ratio ensured complete oxidation of α-pinene during its residence time in the HEC. No NO_x was injected to chamber. The NO and NO_2 were less than 0.5 ppb in the zero air (Aadco Pure Air Generator, model 737).

A sampling outflow was drawn from the center of the bag along the axis perpendicular to both inlet flows. The particle population of this sample passed through a diffusion dryer to remove particle water content and was continuously characterized further downstream by online instrumentation. The particle number concentration of the sampling outflow was measured by a Condensation Particle Counter (CPC, TSI, model 3010).[25] The number-diameter distribution of the dry particle population from 10 to 500 nm was characterized by a Scanning Mobility Particle Sizer (SMPS, TSI, model 3081).[26] Because of the use of the diffusion dryer, variability in diameter due to variable water content was negligible. Dry particle chemical composition was measured by a High-Resolution Time-of-Flight Aerosol Mass Spectrometer (HR-ToF-AMS, Aerodyne).[27,28] The data analysis employed a collection efficiency of 0.5. The HR-ToF-AMS data were processed using standard toolkits (i.e., *SQUIRREL* and *PIKA*),[27,28] and the hydrogen-to-carbon atomic ratio (H:C) and the oxygen-to-carbon atomic ratio (O:C) were determined.[29]

A data set of 52 growth cycles from 0% to 75% RH was collected during the course of the experiments. Except for RH, other parameters, including temperature (22 °C), flow rates, residence time, and α-pinene and ozone injection concentrations, remained the same across the course of the experiments. Table S1 lists further experimental conditions.

2.2. MOSAIC Simulation. The *Model for Simulating Aerosol Interactions and Chemistry* (MOSAIC) is a sectional aerosol box model that simulates new particle production, coagulation, particle-phase thermodynamics, and gas-particle mass transfer of atmospheric trace species.[11,17,30] It dynamically partitions multiple compounds to all particle size bins by considering compound volatility, gas-phase diffusivity, interfacial mass accommodation, molecular diffusion within the interior of the particle, and particle-phase reactions.[11] The thermodynamic driving force for mass transfer is governed by differences between gas-phase mass concentrations and particle-phase saturation concentrations. The kinetic resistance to mass transfer by diffusion within the particle is treated by the two-film theory.[11] Discrete transfer of particle number concentration from one sectional bin to a neighboring bin (i.e., particle growth or shrinkage) takes place due to condensation or evaporation. Particle mass concentration and particle number concentration are conserved.

For the simulations herein, MOSAIC was configured into a continuously mixed flow reactor and defined by the properties of the HEC operation. The approach simulated the growth of the particle population initialized by HEC measurements and grown within an environment of constant gas-phase concentrations of α-pinene ozonolysis products. The concentrations were constant because of the CMFR operation. In the simulation, there were 120 sectional bins, which were spaced logarithmically from 10.6 to 763.1 nm to match the data format of SMPS characterization.

The detailed flowchart for obtaining closure between simulation and observations appears in Figure S2. In that
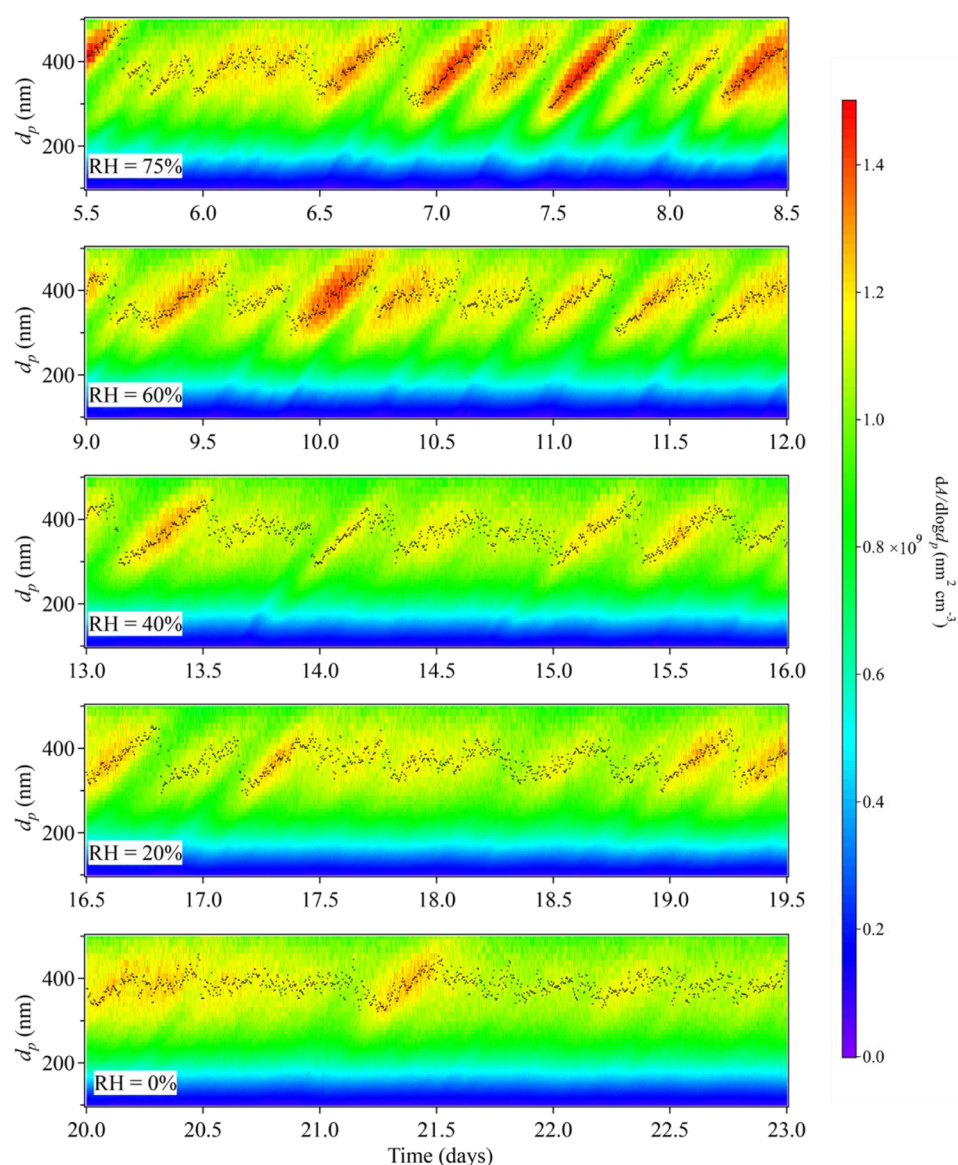
Figure 1. Area-diameter distribution $dA/d\log d_p$ as a function of time t. Black dots represent the mode diameter of the particle population at each time point. Panels are shown for 0% to 75% RH. Conditions: initial α-pinene, 22 ppb; ozone, 350 ppb temperature, 22 °C; chamber residence time, 4.4 h. Days 0 to 5, not shown in the figure, represent a stabilization period in the chamber (Figure S1).

respect, at each RH, the number-diameter distribution observed at the beginning of a growth cycle in the HEC was used to initialize the MOSAIC simulation at time t_0. The initial particles (<10 nm) were treated as internally well mixed because of their production from pure α-pinene ozonolysis products in the absence of any pre-existing inorganic particles. After initialization, particle growth alongside continuous nucleation was simulated for 4 h. The critical nucleated size and nucleation rate were fixed for all simulations. The rate of the continuous nucleation was adjusted to obtain closure between the observed and simulated total number concentrations at 4 h. Coagulation among particles was negligible during the simulation, and condensational growth was the dominant pathway of diameter change.

In the simulation, $C_{g,i}$ values represented how much of the basis-set equivalent of a species i was produced by the VOC oxidation in the HEC. Because the HEC was operated in steady state, the gas-phase concentrations did not change in time,

greatly simplifying the analysis and interpretation. The initial volatility distribution of the oxidation products was estimated by combining the Master Chemical Mechanism[31] and the Simplified Group Contribution[32] (MCM-SIMPOL) and then mapped to the volatility basis set (VBS)[33] (Tables S5). The latter was distributed across decadal saturation concentrations from 10^{-1} to 10^3 μg m^{-3}. The LVOCs were lumped together in the bin with the SVOCs of the lowest saturation vapor pressure. The MCM-SIMPOL VBS served as an initial guess for simulation; the chemistry in MCM is incomplete, and the vapor pressure estimates of SIMPOL are not completely accurate. The $C_{g,i}$ values of the VBS were iterated during the simulation so that there was global convergence to the observed volume concentration across the entire data set. The surface mass accommodation coefficient α of the condensing molecules and their diffusivity D_b in the interior region of the particle (i.e., "bulk" diffusivity) were also iterated so that the simulation matched the observed area-diameter distributions at 4 h.
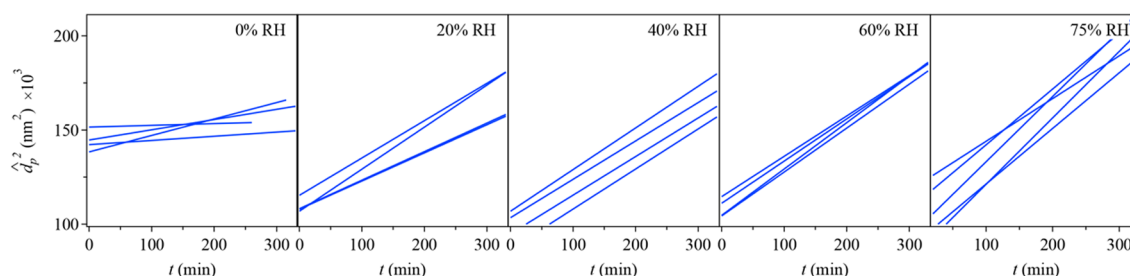
Figure 2. Time series of the square of mode diameter $\hat{d}_p^2$ of the growth profiles of Figure 1. Linear fits to the data are shown for visualization.

3. RESULTS AND DISCUSSION

3.1. Cyclic Particle Growth. The time series of repeating particle growth cycles are plotted in the panels of Figure 1 as area-diameter distributions as a function of time t for 0%, 20%, 40%, 60%, and 75% RH. A cross section of a panel in Figure 1 at fixed time represents the area-diameter distribution $dA/d\log d_p$ for area concentration A and particle diameter d_p. The color legend is shown to the side. Figure 1 represents days 5 to 23 of the experiment after an initial stabilization period of 5 days (Figure S1).

During each growth period, the number concentration of the particle remained in the range of 3200 to 3600 cm^{-3}, and the area concentration varied between $(4.7-5.4)\times 10^8$ nm^2 cm^{-3} for the entire size distribution (Table S1, Figures S1, S3). The explanation for the apparently small variation in these statistics of the particle population is that one nucleation and growth event at its outset accompanied another nucleation and growth event at its tail: the area concentration was dominated by the tail and the number concentration was buffered by new particle production and particle loss. As a result, the number and surface concentrations of the complete particle population (i.e., new + tail) did not increase or decrease significantly along the time axis of the experiment. The mode diameter of the particle population, however, progressively grew to larger sizes across several hours. Across the diameter domain of 200 to 500 nm, in a period of 5 h particle diameters increased by 5−30 nm and 80−140 nm at 0% and 75% RH, respectively. Coagulation between particles was negligible because of the low particle number concentrations ($\ll 10^4$ cm^{-3}, Table S1).[34] Variability in diameter due to variable water content[35] was negligible because of the diffusion dryer inline to the SMPS. The conclusion is that the observed growth in particle diameter corresponded to the condensation of organic molecules.

Warren and Seinfeld[36] describe the CMFR configuration and the protocols typical of a chamber like the HEC as the case of "nucleation and growth of aerosol particles from a continuously reinforced vapor." For cyclic oscillatory nucleation and growth of particles as observed herein, McGraw and Saunders[37] present the mathematics of a condensation feedback mechanism. Thus, a CMFR like the HEC can be operated both in a classic mode in which all species come to steady state but also in an oscillatory mode.

The most important variable in this bifurcation between steady-state and oscillatory modes is the surface area concentration of the particle population for which a low value favors the oscillatory mode. A bit more explanation is as follows. For a CMFR operated with coinjection of a preexisting particle population—which is not the case of the present study—the high surface area concentration can scavenge the low-volatility gas-phase species, produced in situ by the oxidation of VOCs,

and thereby suppress new particle formation from those species. By comparison, in the absence of co-injection (i.e., the experiments described herein), particle nucleation and growth can be persistent and repeated depending on species concentrations, oxidation rates, and chamber operation. Table S2 summarizes the occurrence or the absence of cyclic particle growth in the HEC across several studies and a range of conditions.

In the case of oscillation, the surface area concentration of the nucleated particles never gets large enough to scavenge enough of the continuously produced gas-phase species to fully suppress new particle formation, and nucleation and condensation coexist indefinitely. The relative importance of each at any time point depends on the time-evolving surface area concentration. At any time point, the continuously produced oxidized vapors, originating from the constant reactants fed into the CMFR, contribute in variable balance to the production of nucleated particles or to condensation on the surface of larger particles. Early in the cycle, when the particle surface area concentration is less than the critical point for which most oxidized vapors are scavenged by the particle population, more vapors build up, and there are bursts of new particles. In the middle of the cycle, particles are large enough that vapors are depleted, and the rate of new particle formation is reduced. Late in the cycle, the surface area concentration has an upper limit that crashes because of particle wall loss (which depends on particle size) and chamber residence time. The cycle of particle production and growth begins again.

3.2. Ideal Condensational Growth. For ideal condensational growth, the governing equation for the net condensational flux $J_{c,i}$ of a molecular species i in the continuum regime c is as follows[6]

$$ J_{c,i} = \frac{2\pi D_{g,i}}{M_i} d_p (C_{g,i} - C_{sat,i}) \tag{1} $$

for which $J_{c,i}$ is expressed in moles per time unit. Symbols in eq 1 include the gas-phase diffusivity $D_{g,i}$, the particle diameter d_p, the molecular weight M_i, the gas-phase mass concentration $C_{g,i}$ of species i far away from the particle, and the saturation mass concentration $C_{sat,i}$ just over the particle surface. The latter is related to vapor pressure through the ideal gas law as follows: $C_{sat,i} = (M_i/RT)P_{vap,i}$, where $P_{vap,i}$ is the vapor pressure just over the particle surface, R is the gas constant, and T is the temperature. When Raoult's law holds and the Kelvin effect is omitted, $P_{vap,i} = x_i P_i^0$ where x_i is the mole fraction in the particle and P_i^0 is the vapor pressure over the pure material.

Equation 1 can be modified for Knudsen numbers Kn outside the continuum regime, meaning a mean free path of gaseous molecules that is comparable to or larger than the particle

diameter.[6] When written as diameter change per unit time, the modified equation is as follows

$$I_d = \frac{1}{d_p}\left[\frac{4D_{g,i}}{\rho_p}f(Kn,\alpha)(C_{g,i} - C_{sat.i})\right] = \frac{b}{d_p} \qquad (2)$$

for diameter growth rate I_d. The symbol ρ_p is the material density of the particle. The quantity $f(Kn,\alpha)$ is a correction factor for large Kn and a nonunity mass accommodation coefficient α at the surface. Symbol b, called the growth coefficient, lumps together several quantities. It is given as follows: $b = 4D_{g,i}(C_{g,i} - C_{sat,i})f(kn,\alpha)/\rho_p$. For constant b, integration of eq 2 provides the diameter across time as follows

$$d_p^2 = d_{p,0}^2 + 2bt \qquad (3)$$

for an initial particle diameter $d_{p,0}$. Although $f(Kn,\alpha)$ has a diameter dependence, for simplification, this dependency was omitted in the analysis. The diameter range was similar among the set of conducted experiments so that the numerical error in $f(Kn,\alpha)$ by omission of the diameter dependence was small and thus the attractiveness of the straightforward relation of eq 3 could be retained.

As expected from eq 3, Figure 2 shows that the square $\hat{d}_p^2$ of the mode diameter of the particle population increased linearly over time within a growth cycle. Each line within a panel of Figure 2 represents a successive growth cycle. The slopes of these lines are $2b$. The plots show that the b values are larger for higher RH, increasing from 0.35 to 2.3 nm^2 s^{-1} across 0% to 75% RH. The growth coefficients are plotted as a function of RH in Figure 3.
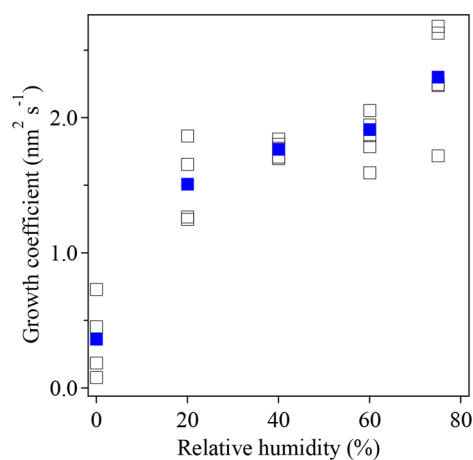

Figure 3. Dependence of growth coefficient b on relative humidity. See eqs 2 and 3 of main text. Open symbols are the slopes of the data sets in Figure 2. Closed symbols are the means of those slopes.

The open symbols correspond to the slopes of the individual trend lines of Figure 2. The closed symbols are the means across those slopes. The plots show that the largest relative change in growth coefficients occurs between 0% and 20% RH. From 20% to 75% RH, the increases are approximately linear with RH. The paramount role of relative humidity for the growth coefficients of the organic particles is apparent. This dependence of b on RH implies nonideal condensational growth.

3.3. Nonideal Condensational Growth. The effects of water on condensational growth through $b(\text{RH})$ can arise from several different possible mechanisms. As a kinetic effect, water can adsorb to the particle surface and modify the mass

accommodation coefficient for condensing molecules, thus altering the growth rate of the particle.[38,39] Water can absorb into the particle and act as a plasticizer to increase the diffusivity of molecules away from the surface region of the particle to the interior of the particle, thereby increasing the growth rate of the particle.[16] As a thermodynamic effect, water can participate in chemical reactions in the gas and particle phases, thereby influencing the mix of oxidation products and hence altering the volatility balance of products and the growth rate of the particles.[40] Particle water can also affect the saturation concentrations and hence volatility balance of the organic species.[41]

For the possible thermodynamic explanation, eqs 2 and 3 of ideal condensational growth still hold, but the parameter values change. Specifically, $C_{g,i}$ is expressed as $C_{g,i}(\text{RH})$. Any change in reaction products $C_{g,i}(\text{RH})$ with RH can be expected to likewise change the chemical composition of the particles with RH. Likewise, significant water uptake into the particles can affect $C_{sat,i}$. In regard to chemical composition, Figure 4a plots the
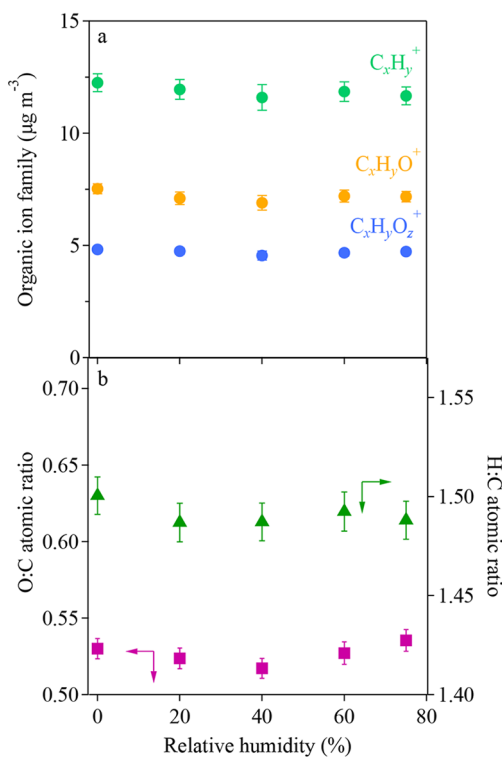

Figure 4. Dependence of chemical composition on relative humidity. (a) Mass concentration of the $C_xH_y^+$, $C_xH_yO^+$, and $C_xH_yO_z^+$ ion families. (b) Oxygen-to-carbon (O:C) and hydrogen-to-carbon (H:C) atomic ratios. Data points represent the average across each panel of Figure 1.

mass concentrations of the $C_xH_y^+$, $C_xH_yO^+$, and $C_xH_yO_z^+$ ion families as a function of RH. Figure 4b plots the oxygen-to-carbon (O:C) and hydrogen-to-carbon (H:C) ratios as a function of RH. These two plots together indicate that neither the ion families nor the atomic ratios substantially changed with RH. In agreement, Li et al.[42] found that the production of highly oxidized molecules did not change with varying RH. Nearly constant O:C, H:C, and fragment ion ratios across different RH values, however, do not necessarily mean that the yields of the VOC oxidation products and the emergent volatility distribution did not vary with RH. In the future, speciated measurements of
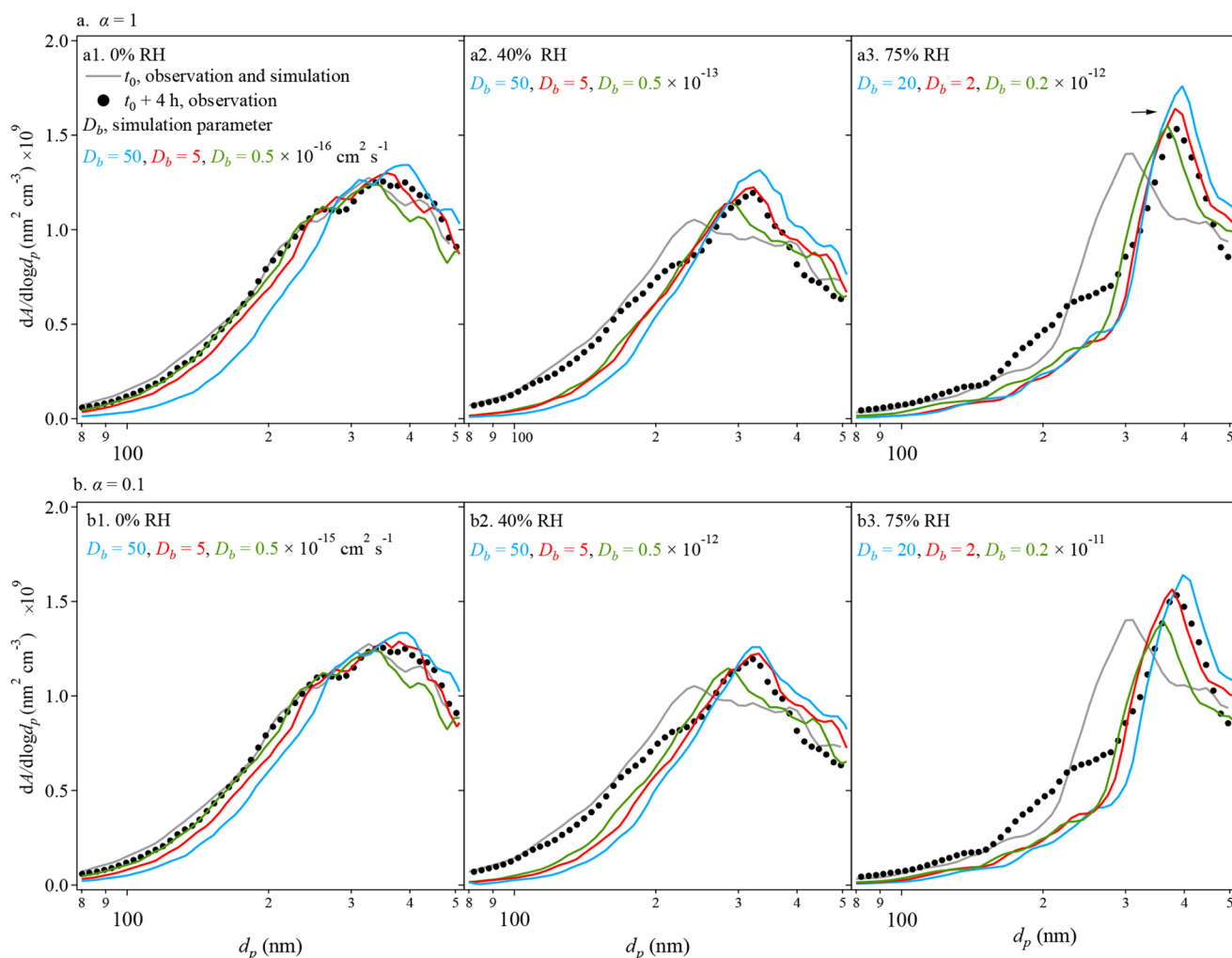
Figure 5. Simulated and measured area-diameter distributions. (a, b) Simulations for $\alpha = 1$ and $\alpha = 0.1$. (1, 2, 3) Simulations for 0%, 40%, and 75% RH. In each panel a1−b3, simulation results after 4 h of growth are shown in color for three different test diffusivities D_b. Gray dots are the distributions observed at t_0 in the HEC and used to initialize the simulation. Black dots are the distributions observed 4 h later in the HEC. Conditions of the simulation correspond to the experiments of Figure 1. Simulations were conducted using the *Model for Simulating Aerosol Interactions and Chemistry* (MOSAIC). Similar plots for 20% and 60% RH appear in Figure S4.

both gas- and particle-phase products can be useful for further insight into this possibility. Zhang et al.,[43] for instance, observed some changes in molecular composition as RH increased from 5% to 55% even as the O:C ratio remained in the range 0.50 ± 0.05. Kristensen et al.[40] likewise observed an increase in dimer concentration at high RH, although the particle mass concentration did not change. The changes observed by Zhang et al. and Kristensen et al. can be important for trace species even as the overall particle composition and the particle mass concentration change negligibly. In agreement, Cocker et al.[44] and Prisle et al.[45] reported that the yield of SOA particle mass concentration from the ozonolysis of α-pinene did not depend on RH. In short, the lack of an RH dependence for $C_xH_y^+$, $C_xH_yO^+$, $C_xH_yO_z^+$, O:C, and H:C shown in Figures 4a and 4b strongly suggests that thermodynamic factors do not well explain the faster growth rates apparent in Figures 3.

As another possibility worthy of consideration, a dependence of wall loss on RH can be considered. Changing amounts of adsorbed water with RH alter the chemical environment of the chamber walls and thereby may affect the deposition of gas-phase species. As an example, the ozone concentration varied by 10% because of RH-dependent wall loss across the studied RH range (Figure S1). Any analogous and significant RH dependence for the wall loss of gas-phase organic species would shift the amount of gas-phase material available for condensation onto the particles and thus influence particle growth rates. In such a case, the growth coefficient should increase at low RH. The data show the opposite trend, however (Figure 3). Moreover, in a continuously mixed flow reactor, species concentrations on walls tend toward an equilibrium saturation, and RH-dependent complications from wall loss are diminished although not entirely eliminated.[23,24,33]

Kinetic inhibition to mass transfer, such as changes in the mass accommodation coefficient or bulk diffusivity, appears a plausible explanation for the dependence of the growth rate on relative humidity. Although the resistance to mass transfer is not directly accounted for in the eqs 1 to 3 of ideal condensational growth, the term $f(Kn,\alpha)$ of eq 2 can be expressed as $f(Kn,\alpha(RH),D_b(RH))$ in full form or $f(RH)$ in short form as a heuristic that does capture nonideal condensational growth while retaining the overall equation of ideal growth.[11] The integrated form of eq 3 continues to hold, and $\hat{d}_p^2$ remains linear in time, although with an RH-dependent slope, as apparent in Figure 2.

The effects of kinetic inhibition on nonideal condensational growth were investigated using the *Model for Simulating Aerosol Interactions and Chemistry* (MOSAIC).[11,17,30,46] The governing equation can be found in the Supporting Information (Text S2), while the detailed framework is presented in Zaveri et al.[11] For each RH, the MOSAIC simulation was initiated with the measured size distribution at time point t_0 of 0 min of Figure 1. Ranges of values of surface mass accommodation coefficients and bulk diffusivities were used across groups of simulations. Particle-phase reactions were not considered in the modeling given that the O:C and H:C ratios did not change across the set of experiments (Figure S1). For each simulation specified by α and D_b, the size distribution was simulated after 4 h of growth (i.e., $t_0 + 4$ h) at each RH. At the end point of each simulation (i.e., $t_0 + 4$ h), the simulated size distributions were compared to the experimental observations. After constraint and optimization to the data sets, the products of the VOC oxidation were distributed in the gas phase prior to any condensation to the particles as follows: 65.9% for $C_{g,0.1}$ where 0.1 represents a volatility of 0.1 μg m^{-3}, 12.5% for $C_{g,1.0}$, 12.5% for $C_{g,10}$, 7.5% for $C_{g,100}$, and 1.6% for $C_{g,1000}$. The volatility distribution is similar to the previous work by Chen et al.[33] but has higher fractional of the lower volatility products. No RH dependence of the $C_{g,i}$ values emerged from the optimization.

Figure 5 shows the initial (gray), final (black), and simulated (color) area-diameter distributions for 0%, 40%, and 75% RH. The color coding represents different decadal values of bulk diffusivity that were used in the simulations. The tested D_b values overestimated (blue), optimally matched (red), or underestimated (green) the observed particle growth. In this way, the kinetic resistance to mass transfer for nonideal condensational growth was quantified by an RH-dependent D_b. For $\alpha = 1$, the optimized D_b values were 5×10^{-16}, 5×10^{-14}, 5×10^{-13}, 1×10^{-12}, 2×10^{-12} cm^2 s^{-1} for 0%, 20%, 40%, 60%, and 75%, respectively. Figure S4 shows the plot for 20% and 60% RH. For $\alpha = 0.1$, the D_b values were 5×10^{-15}, 5×10^{-13}, 5×10^{-12}, 1×10^{-11}, and 2×10^{-11} cm^2 s^{-1} across the range of RH values. In this case, a condensed form is that the D_b values increased from $5 \alpha^{-1} \times 10^{-16}$ for 0% RH to $2 \alpha^{-1} \times 10^{-12}$ cm^{-2} s^{-1} for 75% RH across α values of 0.1 to 1. In agreement with this presentation of a condensed form, in a theoretical study Shiraiwa et al.[47] showed the trade-off between decreasing D_b and increasing $1/\alpha$ as a lumped parameter of the condensational growth rate.

Results are further summarized in Figures 6 and 7. Figure 6 shows a comparison of the measured and simulated growth coefficients as a function of relative humidity. The red symbols represent the best fit between the simulations and the observations (Figure 5). The blue and green symbols represent growth rates that are either too fast or too slow, respectively, to match the laboratory data sets. Figure 7 shows the growth coefficient as a function of bulk diffusivity. Color coding represents relative humidity (see inset legend). The plot shows that the nonideality of the condensational growth can be described by an RH-dependent D_b. Changes in the diffusivity of species in the particle phase result in changes of the growth coefficients by nearly 7-fold from 0% to 75% RH (i.e., b changes from 0.35 to 2.3 nm^2 s^{-1}).

The particle-phase diffusivities obtained herein lie within the range of literature results for α-pinene ozonolysis-derived SOA particles based on a variety of different experimental methods (Figure 8).[16,20,48−51] Similar to the approach herein, He et al.[51] also derived a diffusivity from closure between particle size dynamics and a kinetic model. The study was limited to <5%
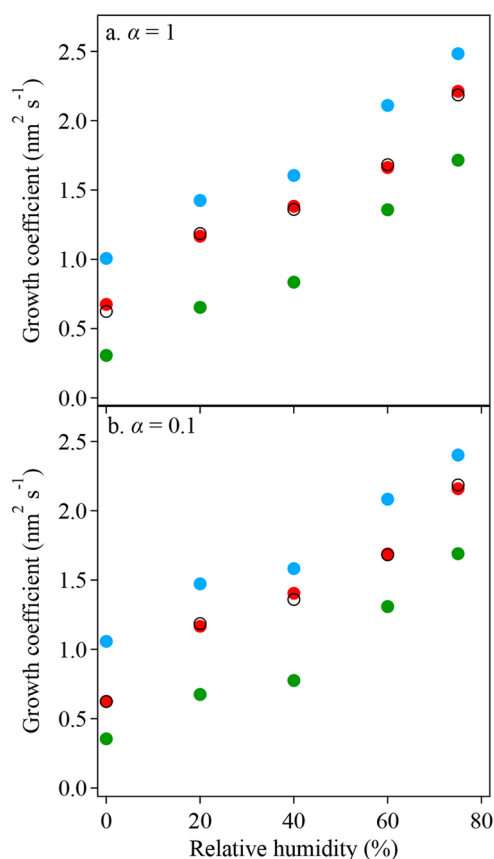

Figure 6. Comparison of measured and simulated growth coefficients as a function of relative humidity. (a, b) Simulations for $\alpha = 1$ and $\alpha = 0.1$. The color code of the closed symbols corresponds to the D_b values of the simulations in each panel of Figure 5 and Figure S4. The open symbols correspond to the experimental observations plotted in Figure 3. The red symbols represent the best fit between simulations and observations.
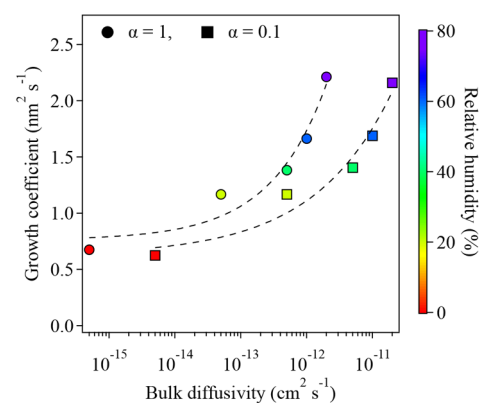

Figure 7. Growth coefficient b as a function of bulk diffusivity. Circles and squares show results for $\alpha = 1$ and $\alpha = 0.1$, respectively. Color coding represents relative humidity (see inset legend). The diffusivity values correspond to the optimized values represented in Figures 5 and 6 by the red coloring.

RH. Liu et al.[16] derived diffusivities from the evaporation rate of organic films. Other studies estimated diffusivities by measuring viscosities and applying the Stokes−Einstein relation.[20,48−50] In respect to the comparisons in Figure 8, some variability in diffusivities among studies is expected because of the uncertainty
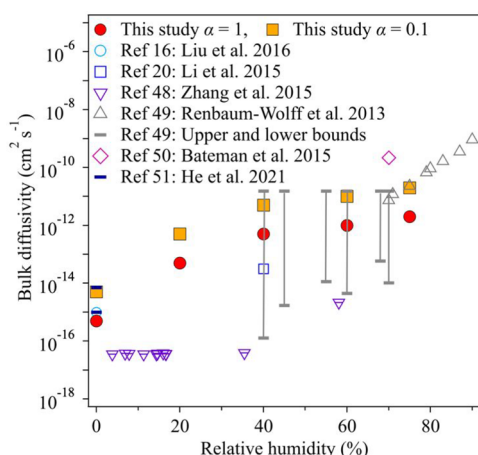
Figure 8. Comparison among the RH-dependent bulk diffusivities of this study and those of other reports in the literature[16,20,48−51] for α-pinene-derived SOA particles.

in the Stokes−Einstein relation and because of the different preparation conditions and oxidation states of the SOA particles.[52,53] As a further example of the latter, for SOA particles produced by hydroxyl radical oxidation of α-pinene in a batch chamber and subsequently photochemically reacted for an additional 16 h, Zaveri et al.[30] estimated bulk diffusivities ranging from 2×10^{-15} at 2% RH to 1×10^{-14} cm^2 s^{-1} at 80% RH for $\alpha = 0.1$. Although the D_b value at low RH is similar to that derived herein for SOA particles produced by ozonolysis of α-pinene for a residence time of 4.4 h, the D_b value at 75% RH is considerably lower. The difference highlights the roles that both the initial oxidation mechanism and the subsequent oxidation chemistry have in the continuous evolution of particle properties during the atmospheric residence time.

In summary, the study herein finds that the condensational growth rate of α-pinene-derived SOA particles increases with RH. A growth coefficient b quantitatively captures the net flux of the condensing molecules toward the particles and accounts for both the thermodynamic driving force and the kinetic resistance of particle growth as a function of RH. The particle chemical composition does not change with RH, suggesting that the thermodynamic driving force is little changed. In this case, the increase in the growth coefficient with RH can be explained by a combination of changes in the mass accommodation coefficient for condensing molecules and diffusivity of those molecules within the particle away from the surface region and into the interior of the particle. The study herein highlights the importance of particle-phase physical properties for the growth rate of the atmospheric aerosol particles and furthers the understanding of the links of atmospheric particles to human health and climate.

ASSOCIATED CONTENT

Supporting Information

The Supporting Information is available free of charge at https://pubs.acs.org/doi/10.1021/acs.est.1c01738.

Description of the MCM-SIMPOL simulation (Text S1), the governing equations for size-dependent gas-particle partitioning in MOSAIC (Text S2), experimental conditions and observations (Table S1), summary of the observations of cyclic growth in the Harvard Environmental Chamber (Table S2), parameters of the MCM-SIMPOL simulation (Table S3), results of the MCM-SIMPOL simulation (Table S4), results of the MCM-SIMPOL simulation represented as a volatility basis set (Table S5), full data set that corresponds to Figure 1 (Figure S1), flowchart of MOSAIC simulation (Figure S2), diagnostic scatter plots of the data sets (Figure S3), and data sets at 20% and 60% RH that complement the data sets shown in Figure 5 (Figure S4) (PDF)

AUTHOR INFORMATION

Corresponding Authors

Scot T. Martin − *School of Engineering and Applied Sciences and Department of Earth and Planetary Sciences, Harvard University, Cambridge, Massachusetts 02138, United States;* orcid.org/0000-0002-8996-7554; Email: scot_martin@harvard.edu

Rahul A. Zaveri − *Atmospheric Sciences and Global Change Division, Pacific Northwest National Laboratory, Richland, Washington 99352, United States;* orcid.org/0000-0001-9874-8807; Email: rahul.zaveri@pnnl.gov

Authors

Yiming Qin − *School of Engineering and Applied Sciences, Harvard University, Cambridge, Massachusetts 02138, United States;* orcid.org/0000-0002-1552-5139

Jianhuai Ye − *School of Engineering and Applied Sciences, Harvard University, Cambridge, Massachusetts 02138, United States;* orcid.org/0000-0002-9063-3260

Paul Ohno − *School of Engineering and Applied Sciences, Harvard University, Cambridge, Massachusetts 02138, United States;* orcid.org/0000-0003-4192-1888

Jinghao Zhai − *School of Engineering and Applied Sciences, Harvard University, Cambridge, Massachusetts 02138, United States; Department of Environmental Science and Engineering, Fudan University, Shanghai 200433, China*

Yuemei Han − *School of Engineering and Applied Sciences, Harvard University, Cambridge, Massachusetts 02138, United States;* orcid.org/0000-0002-5044-8386

Pengfei Liu − *School of Engineering and Applied Sciences, Harvard University, Cambridge, Massachusetts 02138, United States; School of Earth and Atmospheric Sciences, Georgia Institute of Technology, Atlanta, Georgia 30332, United States*

Junfeng Wang − *School of Engineering and Applied Sciences, Harvard University, Cambridge, Massachusetts 02138, United States;* orcid.org/0000-0001-6215-1953

Complete contact information is available at:
https://pubs.acs.org/10.1021/acs.est.1c01738

Author Contributions

S.M. designed the experiments, and Y.Q., J.Z., and Y.H. carried them out. Y.Q. and J.Z. conducted data analysis. Y.Q. and R.A.Z. conducted the MOSAIC simulations. Y.Q. and S.M. wrote the manuscript. J.Y., P.O., P.L., J.W., and R.A.Z. discussed the results and contributed to manuscript editing.

Notes

The authors declare no competing financial interest.
ASCII tab-delimited files of area-diameter distributions of the chamber experiment and the MOSAIC simulations are available at https://doi.org/10.7910/DVN/A7XMG7.

REFERENCES

(1) Tröstl, J.; Chuang, W. K.; Gordon, H.; Heinritzi, M.; Yan, C.; Molteni, U.; Ahlm, L.; Frege, C.; Bianchi, F.; Wagner, R.; Simon, M.; Lehtipalo, K.; Williamson, C.; Craven, J. S.; Duplissy, J.; Adamov, A.; Almeida, J.; Bernhammer, A.-K.; Breitenlechner, M.; Brilke, S.; Dias, A.; Ehrhart, S.; Flagan, R. C.; Franchin, A.; Fuchs, C.; Guida, R.; Gysel, M.; Hansel, A.; Hoyle, C. R.; Jokinen, T.; Junninen, H.; Kangasluoma, J.; Keskinen, H.; Kim, J.; Krapf, M.; Kürten, A.; Laaksonen, A.; Lawler, M.; Leiminger, M.; Mathot, S.; Möhler, O.; Nieminen, T.; Onnela, A.; Petäjä, T.; Piel, F. M.; Miettinen, P.; Rissanen, M. P.; Rondo, L.; Sarnela, N.; Schobesberger, S.; Sengupta, K.; Sipilä, M.; Smith, J. N.; Steiner, G.; Tomè, A.; Virtanen, A.; Wagner, A. C.; Weingartner, E.; Wimmer, D.; Winkler, P. M.; Ye, P.; Carslaw, K. S.; Curtius, J.; Dommen, J.; Kirkby, J.; Kulmala, M.; Riipinen, I.; Worsnop, D. R.; Donahue, N. M.; Baltensperger, U. The role of low-volatility organic compounds in initial particle growth in the atmosphere. *Nature* **2016**, *533*, 527−531.

(2) Vehkamäki, H.; Riipinen, I. Thermodynamics and kinetics of atmospheric aerosol particle formation and growth. *Chem. Soc. Rev.* **2012**, *41*, 5160−5173.

(3) Kodros, J. K.; Volckens, J.; Jathar, S. H.; Pierce, J. R. Ambient particulate matter size distributions drive regional and global variability in particle deposition in the respiratory tract. *GeoHealth* **2018**, *2*, 298−312.

(4) Nemesure, S.; Wagener, R.; Schwartz, S. E. Direct shortwave forcing of climate by the anthropogenic sulfate aerosol: Sensitivity to particle size, composition, and relative humidity. *J. Geophys. Res.* **1995**, *100*, 26105−26116.

(5) Dusek, U.; Frank, G. P.; Hildebrandt, L.; Curtius, J.; Schneider, J.; Walter, S.; Chand, D.; Drewnick, F.; Hings, S.; Jung, D.; Borrmann, S.; Andreae, M. O. Size matters more than chemistry for cloud-nucleating ability of aerosol particles. *Science* **2006**, *312*, 1375−1378.

(6) Seinfeld, J. H.; Pandis, S. N. *Atmospheric Chemistry and Physics: From Air Pollution to Climate Change.* 3rd ed.; Wiley: Hoboken, NJ, 2016.

(7) Jimenez, J. L.; Canagaratna, M. R.; Donahue, N. M.; Prevot, A. S. H.; Zhang, Q.; Kroll, J. H.; DeCarlo, P. F.; Allan, J. D.; Coe, H.; Ng, N. L.; Aiken, A. C.; Docherty, K. S.; Ulbrich, I. M.; Grieshop, A. P.; Robinson, A. L.; Duplissy, J.; Smith, J. D.; Wilson, K. R.; Lanz, V. A.; Hueglin, C.; Sun, Y. L.; Tian, J.; Laaksonen, A.; Raatikainen, T.; Rautiainen, J.; Vaattovaara, P.; Ehn, M.; Kulmala, M.; Tomlinson, J. M.; Collins, D. R.; Cubison, M. J.; Dunlea, J.; Huffman, J. A.; Onasch, T. B.; Alfarra, M. R.; Williams, P. I.; Bower, K.; Kondo, Y.; Schneider, J.; Drewnick, F.; Borrmann, S.; Weimer, S.; Demerjian, K.; Salcedo, D.; Cottrell, L.; Griffin, R.; Takami, A.; Miyoshi, T.; Hatakeyama, S.; Shimono, A.; Sun, J. Y.; Zhang, Y. M.; Dzepina, K.; Kimmel, J. R.; Sueper, D.; Jayne, J. T.; Herndon, S. C.; Trimborn, A. M.; Williams, L. R.; Wood, E. C.; Middlebrook, A. M.; Kolb, C. E.; Baltensperger, U.; Worsnop, D. R. Evolution of organic aerosols in the atmosphere. *Science* **2009**, *326*, 1525−1529.

(8) Donahue, N. M.; Epstein, S. A.; Pandis, S. N.; Robinson, A. L. A two-dimensional volatility basis set: 1. Organic-aerosol mixing thermodynamics. *Atmos. Chem. Phys.* **2011**, *11*, 3303−3318.

(9) Shrivastava, M.; Cappa, C. D.; Fan, J.; Goldstein, A. H.; Guenther, A. B.; Jimenez, J. L.; Kuang, C.; Laskin, A.; Martin, S. T.; Ng, N. L.; Petaja, T.; Pierce, J. R.; Rasch, P. J.; Roldin, P.; Seinfeld, J. H.; Shilling, J.; Smith, J. N.; Thornton, J. A.; Volkamer, R.; Wang, J.; Worsnop, D. R.; Zaveri, R. A.; Zelenyuk, A.; Zhang, Q. Recent advances in understanding secondary organic aerosol: Implications for global climate forcing. *Rev. Geophys.* **2017**, *55*, 509−559.

(10) Han, Y.; Gong, Z.; Ye, J.; Liu, P.; McKinney, K. A.; Martin, S. T. Quantifying the role of the relative humidity-dependent physical state of organic particulate matter in the uptake of semivolatile organic molecules. *Environ. Sci. Technol.* **2019**, *53*, 13209−13218.

(11) Zaveri, R. A.; Easter, R. C.; Shilling, J. E.; Seinfeld, J. H. Modeling kinetic partitioning of secondary organic aerosol and size distribution dynamics: Representing effects of volatility, phase state, and particle-phase reaction. *Atmos. Chem. Phys.* **2014**, *14*, 5153−5181.

(12) Kuwata, M.; Martin, S. T. Particle size distributions following condensational growth in continuous flow aerosol reactors as derived from residence time distributions: Theoretical development and application to secondary organic aerosol. *Aerosol Sci. Technol.* **2012**, *46*, 937−949.

(13) Martin, S. T.; Kuwata, M.; Smith, M. L. An analytic equation for the volume fraction of condensationally grown mixed particles and applications to secondary organic material produced in continuously mixed flow reactors. *Aerosol Sci. Technol.* **2014**, *48*, 803−812.

(14) Gong, Z.; Han, Y.; Liu, P.; Ye, J.; Keutsch, F. N.; McKinney, K. A.; Martin, S. T. Influence of particle physical state on the uptake of medium-sized organic molecules. *Environ. Sci. Technol.* **2018**, *52*, 8381−8389.

(15) Qin, Y.; Ye, J.; Ohno, P. E.; Lei, Y.; Wang, J.; Liu, P.; Thomson, R. J.; Martin, S. T. Synergistic uptake by acidic sulfate particles of gaseous mixtures of glyoxal and pinanediol. *Environ. Sci. Technol.* **2020**, *54*, 11762−11770.

(16) Liu, P.; Li, Y. J.; Wang, Y.; Gilles, M. K.; Zaveri, R. A.; Bertram, A. K.; Martin, S. T. Lability of secondary organic particulate matter. *Proc. Natl. Acad. Sci. U. S. A.* **2016**, *113*, 12643−12648.

(17) Zaveri, R. A.; Shilling, J. E.; Zelenyuk, A.; Liu, J.; Bell, D. M.; D'Ambro, E. L.; Gaston, C. J.; Thornton, J. A.; Laskin, A.; Lin, P.; Wilson, J.; Easter, R. C.; Wang, J.; Bertram, A. K.; Martin, S. T.; Seinfeld, J. H.; Worsnop, D. R. Growth kinetics and size distribution dynamics of viscous secondary organic aerosol. *Environ. Sci. Technol.* **2018**, *52*, 1191−1199.

(18) Bateman, A. P.; Gong, Z.; Liu, P.; Sato, B.; Cirino, G.; Zhang, Y.; Artaxo, P.; Bertram, A. K.; Manzi, A. O.; Rizzo, L. V.; Souza, R. A. F.; Zaveri, R. A.; Martin, S. T. Sub-micrometre particulate matter is primarily in liquid form over amazon rainforest. *Nat. Geosci.* **2016**, *9*, 34−37.

(19) Kuwata, M.; Martin, S. T. Phase of atmospheric secondary organic material affects its reactivity. *Proc. Natl. Acad. Sci. U. S. A.* **2012**, *109*, 17354−17359.

(20) Li, Y. J.; Liu, P.; Gong, Z.; Wang, Y.; Bateman, A. P.; Bergoend, C.; Bertram, A. K.; Martin, S. T. Chemical reactivity and liquid/nonliquid states of secondary organic material. *Environ. Sci. Technol.* **2015**, *49*, 13264−13274.

(21) Perraud, V.; Bruns, E. A.; Ezell, M. J.; Johnson, S. N.; Yu, Y.; Alexander, M. L.; Zelenyuk, A.; Imre, D.; Chang, W. L.; Dabdub, D.; Pankow, J. F.; Finlayson-Pitts, B. J. Nonequilibrium atmospheric secondary organic aerosol formation and growth. *Proc. Natl. Acad. Sci. U. S. A.* **2012**, *109*, 2836−2841.

(22) Zhang, Y.; Liu, P.; Gong, Z.; Geiger, F. M.; Martin, S. T. Production and measurement of organic particulate matter in a flow tube reactor *J. Visualized Exp.* [Online], **2018**. DOI: 10.3791/55684.

(23) Shilling, J. E.; Chen, Q.; King, S. M.; Rosenoern, T.; Kroll, J. H.; Worsnop, D. R.; DeCarlo, P. F.; Aiken, A. C.; Sueper, D.; Jimenez, J. L.;

Martin, S. T. Loading-dependent elemental composition of α-pinene soa particles. *Atmos. Chem. Phys.* **2009**, *9*, 771−782.

(24) Shilling, J. E.; Chen, Q.; King, S. M.; Rosenoern, T.; Kroll, J. H.; Worsnop, D. R.; McKinney, K. A.; Martin, S. T. Particle mass yield in secondary organic aerosol formed by the dark ozonolysis of α-pinene. *Atmos. Chem. Phys.* **2008**, *8*, 2073−2088.

(25) Agarwal, J. K.; Sem, G. J. Continuous flow, single-particle-counting condensation nucleus counter. *J. Aerosol Sci.* **1980**, *11*, 343−357.

(26) Wang, S. C.; Flagan, R. C. Scanning electrical mobility spectrometer. *Aerosol Sci. Technol.* **1990**, *13*, 230−240.

(27) Jayne, J. T.; Leard, D. C.; Zhang, X.; Davidovits, P.; Smith, K. A.; Kolb, C. E.; Worsnop, D. R. Development of an aerosol mass spectrometer for size and composition analysis of submicron particles. *Aerosol Sci. Technol.* **2000**, *33*, 49−70.

(28) DeCarlo, P. F.; Kimmel, J. R.; Trimborn, A.; Northway, M. J.; Jayne, J. T.; Aiken, A. C.; Gonin, M.; Fuhrer, K.; Horvath, T.; Docherty, K. S.; Worsnop, D. R.; Jimenez, J. L. Field-deployable, high-resolution, time-of-flight aerosol mass spectrometer. *Anal. Chem.* **2006**, *78*, 8281−8289.

(29) Canagaratna, M. R.; Jimenez, J. L.; Kroll, J. H.; Chen, Q.; Kessler, S. H.; Massoli, P.; Hildebrandt Ruiz, L.; Fortner, E.; Williams, L. R.; Wilson, K. R.; Surratt, J. D.; Donahue, N. M.; Jayne, J. T.; Worsnop, D. R. Elemental ratio measurements of organic compounds using aerosol mass spectrometry: Characterization, improved calibration, and implications. *Atmos. Chem. Phys.* **2015**, *15*, 253−272.

(30) Zaveri, R. A.; Shilling, J. E.; Zelenyuk, A.; Zawadowicz, M. A.; Suski, K.; China, S.; Bell, D. M.; Veghte, D.; Laskin, A. Particle-phase diffusion modulates partitioning of semivolatile organic compounds to aged secondary organic aerosol. *Environ. Sci. Technol.* **2020**, *54*, 2595−2605.

(31) Jenkin, M. E.; Saunders, S. M.; Wagner, V.; Pilling, M. J. Protocol for the development of the master chemical mechanism, MCM v3 (Part b): Tropospheric degradation of aromatic volatile organic compounds. *Atmos. Chem. Phys.* **2003**, *3*, 181−193.

(32) Pankow, J. F.; Asher, W. E. Simpol.1: A simple group contribution method for predicting vapor pressures and enthalpies of vaporization of multifunctional organic compounds. *Atmos. Chem. Phys.* **2008**, *8*, 2773−2796.

(33) Chen, Q.; Liu, Y.; Donahue, N. M.; Shilling, J. E.; Martin, S. T. Particle-phase chemistry of secondary organic material: Modeled compared to measured O:C and H:C elemental ratios provide constraints. *Environ. Sci. Technol.* **2011**, *45*, 4763−4770.

(34) Kerminen, V.-M.; Chen, X.; Vakkari, V.; Petäjä, T.; Kulmala, M.; Bianchi, F. Atmospheric new particle formation and growth: Review of field observations. *Environ. Res. Lett.* **2018**, *13*, 103003.

(35) Varutbangkul, V.; Brechtel, F. J.; Bahreini, R.; Ng, N. L.; Keywood, M. D.; Kroll, J. H.; Flagan, R. C.; Seinfeld, J. H.; Lee, A.; Goldstein, A. H. Hygroscopicity of secondary organic aerosols formed by oxidation of cycloalkenes, monoterpenes, sesquiterpenes, and related compounds. *Atmos. Chem. Phys.* **2006**, *6*, 2367−2388.

(36) Warren, D. R.; Seinfeld, J. H. Nucleation and growth of aerosol from a continuously reinforced vapor. *Aerosol Sci. Technol.* **1984**, *3*, 135−153.

(37) McGraw, R.; Saunders, J. H. A condensation feedback mechanism for oscillatory nucleation and growth. *Aerosol Sci. Technol.* **1984**, *3*, 367−380.

(38) Julin, J.; Winkler, P. M.; Donahue, N. M.; Wagner, P. E.; Riipinen, I. Near-unity mass accommodation coefficient of organic molecules of varying structure. *Environ. Sci. Technol.* **2014**, *48*, 12083−12089.

(39) Liu, X.; Day, D. A.; Krechmer, J. E.; Brown, W.; Peng, Z.; Ziemann, P. J.; Jimenez, J. L. Direct measurements of semi-volatile organic compound dynamics show near-unity mass accommodation coefficients for diverse aerosols. *Commun. Chem.* **2019**, *2*, 98.

(40) Kristensen, K.; Cui, T.; Zhang, H.; Gold, A.; Glasius, M.; Surratt, J. D. Dimers in α-pinene secondary organic aerosol: Effect of hydroxyl radical, ozone, relative humidity and aerosol acidity. *Atmos. Chem. Phys.* **2014**, *14*, 4201−4218.

(41) Pankow, J. F.; Marks, M. C.; Barsanti, K. C.; Mahmud, A.; Asher, W. E.; Li, J.; Ying, Q.; Jathar, S. H.; Kleeman, M. J. Molecular view modeling of atmospheric organic particulate matter: Incorporating molecular structure and co-condensation of water. *Atmos. Environ.* **2015**, *122*, 400−408.

(42) Li, X.; Chee, S.; Hao, J.; Abbatt, J. P. D.; Jiang, J.; Smith, J. N. Relative humidity effect on the formation of highly oxidized molecules and new particles during monoterpene oxidation. *Atmos. Chem. Phys.* **2019**, *19*, 1555−1570.

(43) Zhang, X.; McVay, R. C.; Huang, D. D.; Dalleska, N. F.; Aumont, B.; Flagan, R. C.; Seinfeld, J. H. Formation and evolution of molecular products in α-pinene secondary organic aerosol. *Proc. Natl. Acad. Sci. U. S. A.* **2015**, *112*, 14168−14173.

(44) Cocker, D. R., III; Clegg, S. L.; Flagan, R. C.; Seinfeld, J. H. The effect of water on gas-particle partitioning of secondary organic aerosol. Part I: A-pinene/ozone system. *Atmos. Environ.* **2001**, *35*, 6049−6072.

(45) Prisle, N. L.; Engelhart, G. J.; Bilde, M.; Donahue, N. M. Humidity influence on gas-particle phase partitioning of α-pinene + O_3 secondary organic aerosol. *Geophys. Res. Lett.* **2010**, *37*, L01802.

(46) Zaveri, R. A.; Easter, R. C.; Fast, J. D.; Peters, L. K. Model for simulating aerosol interactions and chemistry (MOSAIC). *J. Geophys. Res.* **2008**, *113*, D13204.

(47) Shiraiwa, M.; Pöschl, U. Mass accommodation and gas-particle partitioning in secondary organic aerosols: Dependence on diffusivity, volatility, particle-phase reactions, and penetration depth. *Atmos. Chem. Phys.* **2021**, *21*, 1565−1580.

(48) Zhang, Y.; Sanchez, M. S.; Douet, C.; Wang, Y.; Bateman, A. P.; Gong, Z.; Kuwata, M.; Renbaum-Wolff, L.; Sato, B. B.; Liu, P. F.; Bertram, A. K.; Geiger, F. M.; Martin, S. T. Changing shapes and implied viscosities of suspended submicron particles. *Atmos. Chem. Phys.* **2015**, *15*, 7819−7829.

(49) Renbaum-Wolff, L.; Grayson, J. W.; Bateman, A. P.; Kuwata, M.; Sellier, M.; Murray, B. J.; Shilling, J. E.; Martin, S. T.; Bertram, A. K. Viscosity of α-pinene secondary organic material and implications for particle growth and reactivity. *Proc. Natl. Acad. Sci. U. S. A.* **2013**, *110*, 8014−8019.

(50) Bateman, A. P.; Bertram, A. K.; Martin, S. T. Hygroscopic influence on the semisolid-to-liquid transition of secondary organic materials. *J. Phys. Chem. A* **2015**, *119*, 4386−4395.

(51) He, Y.; Akherati, A.; Nah, T.; Ng, N. L.; Garofalo, L. A.; Farmer, D. K.; Shiraiwa, M.; Zaveri, R. A.; Cappa, C. D.; Pierce, J. R.; Jathar, S. H. Particle size distribution dynamics can help constrain the phase state of secondary organic aerosol. *Environ. Sci. Technol.* **2021**, *55*, 1466.

(52) Evoy, E.; Maclean, A. M.; Rovelli, G.; Li, Y.; Tsimpidi, A. P.; Karydis, V. A.; Kamal, S.; Lelieveld, J.; Shiraiwa, M.; Reid, J. P.; Bertram, A. K. Predictions of diffusion rates of large organic molecules in secondary organic aerosols using the Stokes-Einstein and fractional Stokes-Einstein relations. *Atmos. Chem. Phys.* **2019**, *19*, 10073−10085.

(53) Grayson, J. W.; Zhang, Y.; Mutzel, A.; Renbaum-Wolff, L.; Böge, O.; Kamal, S.; Herrmann, H.; Martin, S. T.; Bertram, A. K. Effect of varying experimental conditions on the viscosity of α-pinene derived secondary organic material. *Atmos. Chem. Phys.* **2016**, *16*, 6027−6040.